Acta Materialia 195 (2020) 1–11

Contents lists available at ScienceDirect

Acta Materialia

journal homepage: www.elsevier.com/locate/actamat

A combined compression and indentation study of mechanical metamaterials based on inverse opal coatings

Jefferson J. do Rosário[a], Yen Häntsch[a], Gerold A. Schneider[a], Erica T. Lilleodden[a,b,*]

[a] Institute of Advanced Ceramics, Hamburg University of Technology, Denickestrasse 15, D-21073 Hamburg, Germany
[b] Institute of Materials Research, Materials Mechanics, Helmholtz-Zentrum Geesthacht, Max-Planck-Strasse 1, D-21502 Geesthacht, Germany

ARTICLE INFO

Article History:
Received 12 December 2019
Revised 8 April 2020
Accepted 11 April 2020
Available online 12 May 2020

Keywords:
Nanoindentation
Metamaterials
Mechanical properties
Porous

A relatively new class of tailored photonic metamaterials based on the inverse opal (IO) structure shows multifunctionality with exceptional mechanical response due to its periodic porous arch-like structure. Exploiting the smaller is stronger paradigm through varying its pore size and the addition of atomic layer deposition (ALD) films, allow tailorable strength and elastic modulus. Quantification of such properties are achieved through flat punch nanoindentation testing. Results are validated by comparison to microcompression tests, a widely used technique to circumvent the complex stress state normally imposed by indentation, but in the case of high porosity is greatly simplified, approximating uniaxial stress; results from both mechanical loading approaches show strong similarities. All results showed a dependence of strength and elastic modulus on the ratio of the deformation size, i.e., micropillar or flat punch diameter, to the pore size, a trend which is well described by the influence of the boundary conditions of the test method rather than an intrinsic size effect. At larger ratios the values approach a constant value. Furthermore, the mechanical response can be tailored through the deposition of a thin film on the shell structure of the silica IO structures; 34 nm of TiO_2 was shown to produce a 10-fold increase in strength and 5-fold increase in elastic modulus.

1. Introduction

Mechanical metamaterials, a relatively new class of porous materials in which the mechanical properties are largely governed by structural geometry rather than composition, are artificially designed to present mechanical properties not always found in nature, analogous to electromagnetic, acoustic and photonic metamaterials. Recent developments in fabricating such nano-scaled porous structures has led to optimizing multi-functionality through the significant increase in surface area to volume ratio, the exploitation of the "smaller is stronger" paradigm [1–6], and through the utilization of length-scales allowing unique functionality such as photonic response [7] and energy absorption properties [8]. Top-down approaches have received perhaps the most attention, in which truss structures are achieved through different laser-lithography method [1–6,8–12]. Many of these fabricated structures are based on the octet-truss – a strut-based design material with an FCC lattice [1–4,10,11], suggested by Deshpande et al. [13,14] due to its stretching dominated architecture. Other designs, such as honeycombs [3,5] and bending dominated lattices [3,5,8,9] have also been explored. While many of these materials have displayed outstanding properties, a lack of mass production techniques is a severe limitation to their utility. An alternative approach utilizes self-assembly of nano- or micro-particles, is relatively inexpensive and offers the potential for mass production. We recently introduced such a strategy for fabricating mechanical metamaterials based on the inverse opal (IO) structure [7,15], and showed that these unique multifunctional materials exhibit exceptional mechanical response due to its periodic porous arch-like structure. Such structures are currently limited to coatings in the sub-millimetre dimension, but can be used for large surface coverage, e.g. several cm^2 are easy achieved, and simultaneously offer tunable photonic properties.

The dimensions and high intrinsic compliance of such structures limits the use of traditional testing techniques to characterize their mechanical response. On the one hand, micro-compression testing has gained favor for assessing the mechanical behavior of lithographically prepared truss structures, but in the case of coatings covering large areas, the technique suffers from potential artefacts (e.g. redeposition, microstructural changes) and lack of efficiency associated with the needed focused ion beam (FIB) milling preparation of micropillars. On the other hand, indentation is typically considered a complicated approach for assessing quantitative constitutive behavior, owing to the imposed gradients in stress and the sensitivity to the underlying material. However, in the case of porous materials, the use of indentation methods may be more straightforward relative to fully dense materials. Especially in the case of porous coatings on

* Corresponding author at: Institute of Advanced Ceramics, Hamburg University of Technology, Denickestrasse 15, D-21073 Hamburg, Germany.
E-mail address: erica.lilleodden@hzg.de (E.T. Lilleodden).

https://doi.org/10.1016/j.actamat.2020.04.025

relatively stiff, hard substrates, the use of flat ended punch indenters can lead to a nominally uniaxial stress state, simplifying the characterization and its analysis.

Here we aim to understand the coupled influences of loading approach – namely indentation and compression testing – and the relative microstructural and geometric length-scales on the elastic modulus and strength of inverse opal structures of varying pore size and with and without a reinforcing amorphous titania film. Importantly, through the comparison of results from flat punch indentation and microcompression testing, we aim to establish the validity of flat punch indentation for the quantification of uniaxial mechanical behaviour of materials with high porosity and limited structural dimensions, i.e., coatings. This would be highly advantageous since flat punch indentation is a far more efficient mechanical testing technique with higher statistical robustness compared to compression testing, and importantly does not suffer from the usual artefacts due to sample preparation via FIB milling.

2. Experimental procedures

2.1. Inverse opal fabrication and structural characterization

Silica IOs were fabricated based by a co-assembly process developed by Hatton et al. [16]. Water based suspensions were prepared from a mixture of 5 or 10 w/v% stock suspension of commercial monodisperse polystyrene (PS) spheres (Microparticles GmbH) and hydrolyzed TEOS (Tetraethyl orthosilicate) solution. The diameters of polymer spheres used were 198 ± 5, 522 ± 12, 756 ± 20 and 1030 ± 40 nm as stated by the supplier. The TEOS solution was composed of 1:1:1.5 ratio by weight of TEOS, 0.10 M HCl and EtOH stirred for 1 h. The final suspension contained 0.6 or 1.2 mL of PS stock (for stocks suspensions of 10 w/v% and 5 w/v%, respectively) and 0.450 mL of hydrolyzed TEOS solution in a final volume of 50 mL. Soda-lime silica glass substrates (25 mm x 75 mm) were cleaned by soaking in alkaline detergent solution (Mucasol, Merz Hygiene GmbH), brushing, rinsing with hot tap water and deionized water, blow dried with filtered nitrogen and oxygen-plasma cleaned (Polaron PT7160 RF, Quorum Technologies Ltd) with 100 W for 20 min prior using. The cleaned substrates were vertically placed in beakers containing the final suspension. The solvent was slowly evaporated in a humidity chamber at 60 °C for 3 to 5 days (grown rate of 0.5 cm/day) for the growing of the composite of PS and silica on the substrate. After drying the deposited coating at room temperature, the PS template was removed by annealing the structure at 500 °C for 30 min with a heating rate of 1 °C min^{-1}, resulting in the desired silica inverse opal.

Inverse opals from template PS spheres of 756 nm were subsequently coated by atomic layer deposition (ALD) with a thin layer of amorphous titania of approx. 34 nm. The ALD process was carried out in a custom-made ALD reactor performing under exposure mode to ensure conformal film. Therefore, alternating pulses of the precursor titanium tetraisopropoxide (TTIP) for 2 s and water vapor for 0.4 s were selected where after each pulse a long exposure of 60 s and then 90 s N_2 purge was done to first achieve complete coverage of all surface sites and then remove unreacted precursor and byproducts. The ALD-film thickness was measured in a spectroscopic ellipsometer from a thin titania layer deposited on a silicon wafer during the same ALD process. The size of the pores of the inverse opals is referred throughout this work as the size of the PS template used for its fabrication.

The specular reflectance of the IOs was measured at 8° from 250 nm to 2000 nm in wavelength using Perkin-Elmer UV/Vis/NIR Lambda 19 spectrometer. XRD measurements (Bruker AXS D8 Discover) were performed with Cu-Kα radiation using a LynxEye detector in 1D mode and pseudo-Bragg-Brentano geometry. XRD diffractograms were matched to PDFs from the ICDD. The diffractograms shown in the Supplementary Information Fig. S1 confirm the deposition of an amorphous titania film via ALD.

The structure of IO coatings, pillars and indents was investigated by scanning electron microscopy (SEM, Leo 1530 Gemini and Zeiss Supra 55 VP, Carl Zeiss Microscopy). Top down SEM images are used to compute the top cross-sectional area. While side-views of the pillars could be used to measure the height of the column and cleavage of the samples near to the indents used to measure the height of the coating. However, errors associated with the combined tilted view and slight taper of the pillar or irregularities in the coating cleavage plane can lead to significant errors in the measurement of height. Therefore the height was alternatively computed from the known FCC structure of the IO in combination with the SEM images. For an FCC crystal the height, H, in the <111> direction is given by:

$$H = N_{layers}\frac{\sqrt{3}}{3}\sqrt{2}D \quad (1)$$

where N_{layers} is the number of (111) layers, and D is the diameter of the spherical pore.

Fig. 1a–d shows surface images of IOs with different pore sizes fabricated with polymer spheres templates with 198, 522, 756 and 1030 nm in diameter, respectively. Additionally, Fig. 1c shows the IO from 756 nm template spheres before and after the deposition of a 34 nm amorphous TiO_2-film. The surface of a self-assembled FCC-opal consist of the (111) plane, the plane with highest packing density. The three darker holes on the bottom of each pore show the connection with the next plane of pores. For the central sample of this study, the IO from 756 nm template spheres, the final structure is an inverted FCC elliptical structure with pore size of 725 nm parallel to the substrate and 670 nm perpendicular to the substrate. The deformation arises from an anisotropic shrinkage upon calcination. The pores are interconnected by holes of approx. 170 nm in diameter. Comparing the same IO before and after TiO_2-film (Fig. 1c) it can be observed that the templated pores and the connection holes are considerably smaller after film deposition.

Due to the fabrication method, the thicknesses of the IO coatings vary over the deposition process. For opals with pore size of 756 nm, the measurement of thicknesses was performed from the FIB'd pillars. Pure silica IO and silica IO coated with 34 nm TiO_2 have 8.5 and 5.5 layers of pores along the <111> direction, yielding heights of 4.7 μm and 3.0 μm, respectively. For IOs with a template sphere size of 198, 522 and 1030 nm, the coating thickness was measured by direct imaging of cleaved cross section of the samples near to indentation measurements. The samples presented 15.5, 13.5 and 4.5 layers of pores, yielding heights (considering around 11% shrinkage along the <111> direction) of 2.2 μm, 5.1 and 3.4 μm, respectively. Comparing these values to the estimates from the SEM images, we find excellent agreement.

Fig. 1e shows the specular reflection measurements of the pure silica inverse opals fabricated with template pores of 198 nm, 522 nm, 756 nm and 1030 nm, along with the silica inverse opal fabricated with template pore of 756 nm coated with 34 nm of titania. These layers present characteristic photonic stop-gaps, which have an expected red shift with the increase of pore size. Shang et al. [17] reported a characteristic red shift after atomic layer deposition of conformal titania film with different thicknesses on opal coatings for simulated reflectance spectra as well as for experimental spectra. Here, the effect of the titania film can also be observed in the photonic stop-gap by a red shift and intensity increase associated to the addition of a material with higher refractive index; results are consistent with a film thickness of 34 nm.

2.2. Mechanical characterization

In order to investigate the mechanical response of these highly porous materials, two types of indentation-based experiments were

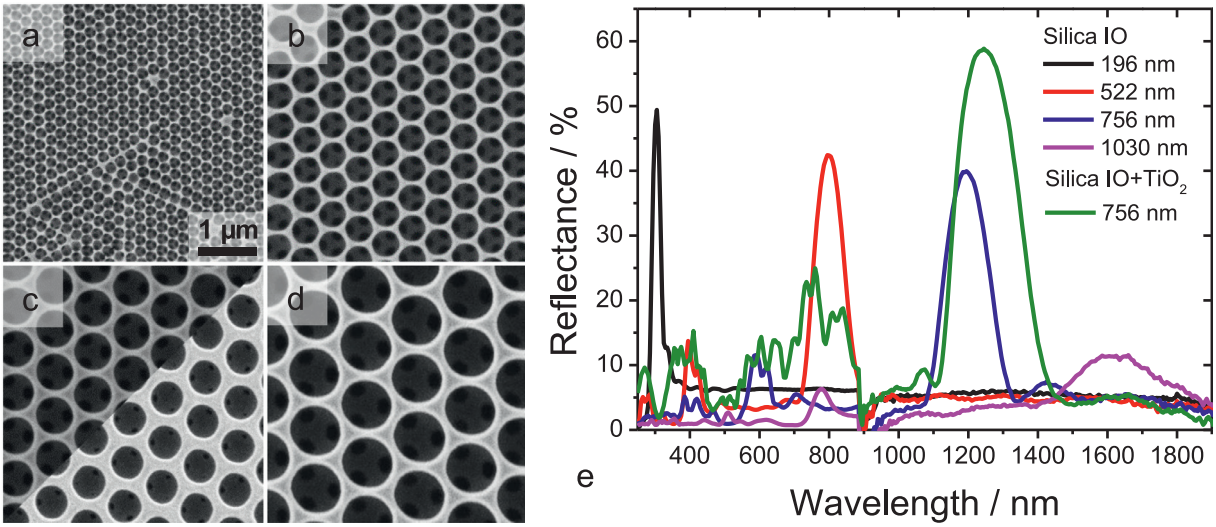

Fig. 1. Samples. SEM images of the surface of inverse opals fabricated with template spheres of a) 198 nm, b) 522 nm, c) 756 nm and d) 1030 nm. In (c) the inverse opal fabricated with template spheres of 756 nm is shown before (pure silica, upper left region) and after ALD of 34 nm of titania (lower right region), where the slightly smaller pores and connecting holes are clearly visible. e) Specular reflection measurements of the pure silica inverse opals fabricated with template pores of 198 nm, 522 nm, 756 nm and 1030 nm and silica inverse opal fabricated with template pore of 756 nm coated with 34 nm of titania.

carried out using a Nanoindenter XP (MTS Corp.): namely, microcompression and flat-punch indentation. Microcompression tests were carried out on silica IO samples with a nominal pore spacing of 756 nm, with and without the 34 nm titania film. Micropillars with rectangular cross sections were fabricated by focused ion beam (FIB) milling using a Nanolab 200 DualBeam microscope (FEI Corp., now Thermo-Fischer). A cleaning cross section milling protocol using 300 pA current and 30 kV accelerating voltage was carried out as the final milling step on all surfaces. Minimal exposure of the fabricated pillars to the Ga ion beam was achieved since no direct imaging of the structure with the ion beam was required. By milling all pillars to heights beyond the IO coating thickness the underlying glass substrate serves as a stiff and hard platen. Here, the deformation is strongly limited to the IO coating, with a single deformation volume and in turn a straightforward analysis of the uniaxial stress-strain response. This is a major advantage of testing micropillars fabricated from coating materials, rather than micropillars from bulk materials. The equivalent diameter of cross sections of the pillars were varied, with size ranges of about 2 μm to about 20 μm, while the height is dictated by the coating thickness. As will be discussed later, the smallest pillars and largest pore sizes suffer from redeposition of material during FIB milling.

In the case of flat-punch indentation, 60° conical indenters with nominally circular flat ends of varying diameter were used. The size of the flat punch is expressed as an equivalent diameter, to accommodate the imperfect circular ended indenters. The sizes were measured from SEM images of residual indents, on both the opal structures as well as on a standard aluminium single crystalline samples. Punches with equivalent diameters of 2.5, 5.5, 10.7, 15.1, 19.4 and 54.5 μm were used. Due to the microstructural length scale of the samples, 2.5 μm was the smallest punch diameter employed, and due to the coating thicknesses of less than 5 μm combined with the importance of good alignment between the punch and the sample, 54.5 μm was the largest punch diameter employed. Indentation tests were also carried out on the IOs with different pore sizes.

In order to compare all data, a parameter is introduced to consider the relative geometrical length scale, D_G, taken as the equivalent diameter of either the pillar or flat punch, and the microstructural length scale, D_μ, taken as the pore spacing. The ratio D_G/D_μ, is used herein as a key parameter in the analyses of all results. An overview of the experimental approach used in this work is shown in Fig. 2.

Compression and indentation tests were carried out using the same loading protocol. A constant displacement rate of 10 nm s^{-1} was used, with an imposed 2 nm displacement oscillation amplitude at a frequency of 45 Hz in order to provide a continuous measurement of the elastic contact stiffness (CSM) from which the elastic modulus can be computed all along the loading curve. Partial unloading segments carried out at a nominal depth of 200 nm were included in many of the tests in order to evaluate the quasi-static contact stiffness. The prescribed maximum displacement was varied. However, as will be discussed, instabilities in mechanical response often led to overshooting of this displacement. Careful alignment of the indenter and sample surface allowed an even pressure distribution across the contact area. In the case of flat punch indentation, this alignment was confirmed by SEM imaging of the contact perimeter after indentation.

In the case of microcompression, the stress, σ, is computed as the load, P, divided by the top cross sectional area of the pillars. The strain, ε, was computed as $\varepsilon = h/H$, where h is the indentation displacement and H is the height of the pillars, which is equivalent to the thickness of the coating. The elastic modulus was computed by the loading slope, dP/dh, and by the continuous stiffness measurement, S_{CSM}, as $E_{loading} = (dP/dh)\,(H/A)$ and $E_{CSM} = S_{CSM}\,(H/A)$, respectively. For simplicity, compensation of the elastic displacements of the underlying soda-lime glass substrate are neglected since its modulus is nearly 10 times greater than that of the inverse opal. This leads to a slight overestimation of the strain and in turn leads to a slight underestimation of the modulus; the stress is not affected. We note that the modulus measured in the experiments is that in the <111> direction of the IO structure.

In the case of flat punch indentation, an analysis of the stress–-strain response is not readily defined. A mean pressure is used as a proxy for stress, and is computed as the load divided by the area of contact. Despite the conical shape of the indenter side walls, the contact area can be taken as that of the circular flat within the elastic regime. While a uniform strain can not be computed from indentation in fully dense solids due to the long-range, gradient stress field, in the case of porous coatings on relatively rigid substrates, an equivalency to uniaxial compression might be exploited. Likewise, the assessment of elastic modulus must be carefully considered, as the usual application of the Sneddon solution, $E_{Sneddon} = (S_{CSM}/D_{contact})$, where $D_{contact}$ is the diameter of the contact area, assumes a

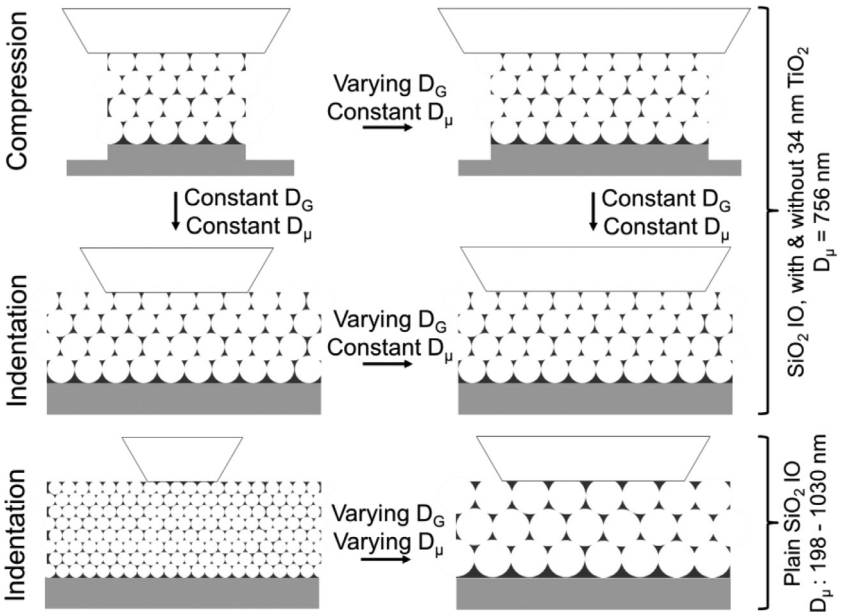

Fig. 2. Experimental approach. Schematic of the experimental approaches used herein, namely compression and indentation applied to IOs of varying deformation volume and pore size.

homogeneous half space. Again, an equivalence to uniaxial compression might be used. This will be explored and discussed further in the results and discussion sections.

3. Results

3.1. Compression

Microcompression experiments conducted on uncoated silica IO structures of varying micropillar diameters displayed fairly linear elastic loading up to a critical stress at which point – or shortly thereafter - catastrophic failure occurs. Representative load vs displacement curves and associated micrographs of pillars before and after loading are shown in Fig. 3. Despite using a prescribed maximum displacement of 700 nm, catastrophic failure of the uncoated IO pillars always resulted, as signified by a large displacement burst and a crushed post-compression structure. Results from microcompression tests on the titania coated IO structures showed significantly higher loads at failure, and did not lead to catastrophic fracture as found in the uncoated system (Fig. 4); despite massive deformation and fracture, the IO coating remains largely intact on the top surface. Further SEM images of micropillars with varying diameters of the silica IOs with and without a titania film, before and after compression tests are shown in the Supplementary Information Figs. S2 and S3.

Using the analyses described in Section 2.2, the stress vs strain response was computed from the load-displacement data (Figs. S4–S6). A critical stress can be identified from the point of failure, and the elastic modulus was assessed from the loading curve as well as from the continuous stiffness measurements. The results for all microcompression experiments are provided in Table 1. In all cases, the results from the continuous stiffness measurement analysis of elastic modulus is slightly higher than that computed from the loading slope.

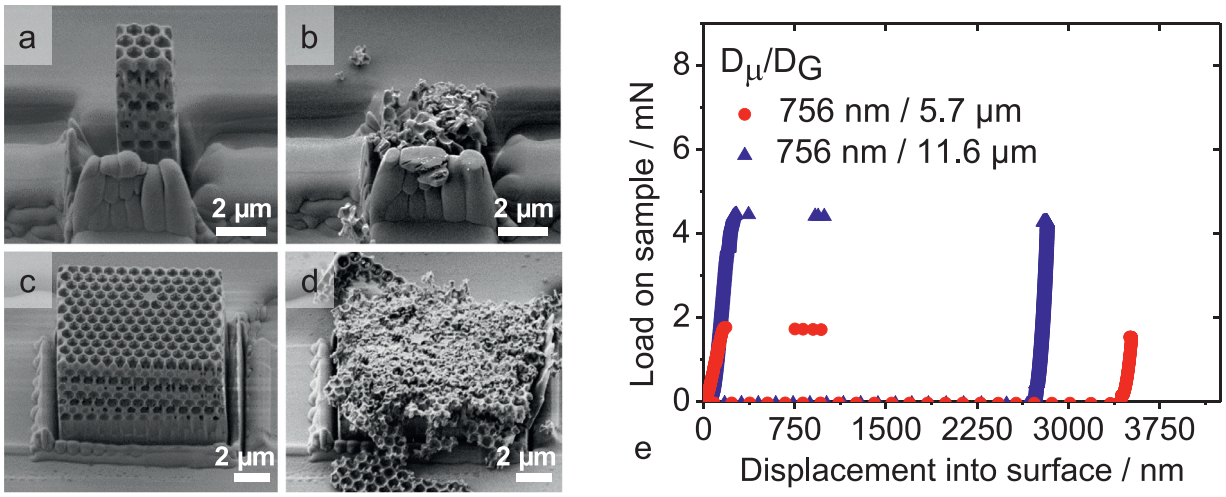

Fig. 3. Results from microcompression of uncoated IO. Typical micropillars fabricated by FIB, shown as fabricated (left) and after compression tests (right). Uncoated silica inverse opals fabricated with polymer template spheres of D_μ = 756 nm with pillar cross section diameter of a,b) D_G = 2 μm and c,d) D_G = 11 μm. e) Typical load-displacement curves for D_μ = 756 nm and varying D_G.

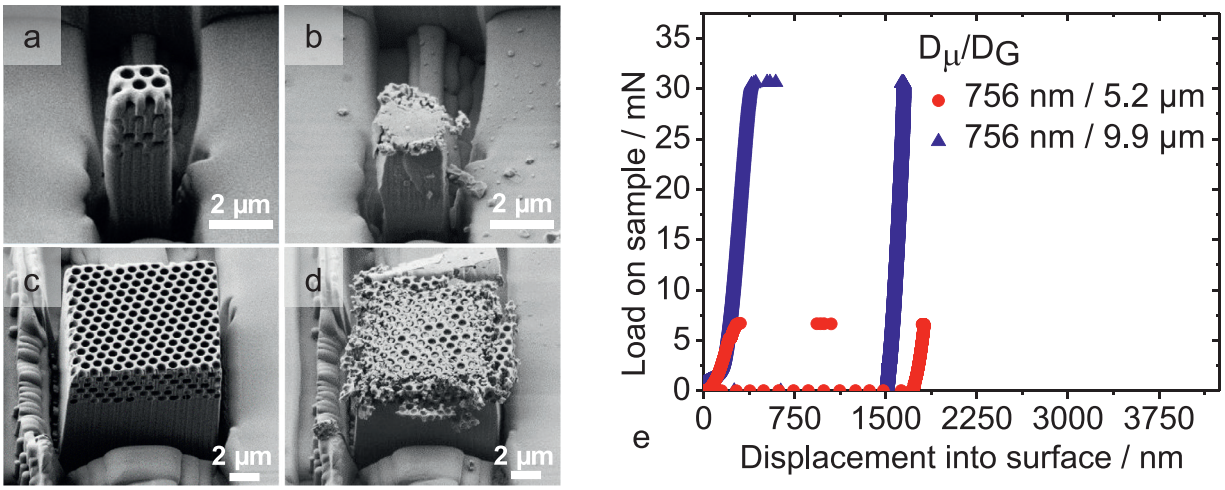

Fig. 4. Results from microcompression of coated IO. SEM images of micropillars from silica IO coated with 34 nm amorphous titania before (a,c) and after (b,d) compression tests. Significant redeposition of material due to FIB milling is observed in (a). The polymer template sphere size is D_μ = 756 nm and the pillar cross section diameter is D_G = 2 μm (a,b) and D_G = 10 μm (c,d). e) Typical load-displacement curves of coated silica IO for D_μ = 756 nm and varying D_G.

This is expected, and reveals some non-linear deformation during loading.

3.2. Flat punch indentation

Figs. 5 and 6 present typical results from the flat punch indentation experiments on the uncoated and coated IO structures, respectively, along with residual impressions from indentations into structures with varying pore size D_μ and punch diameter D_G. Fig. 5b shows 4 load-displacement curves for the uncoated structures. 2 curves are associated with a pore sizes of D_μ= 756 nm and flat punch diameter of D_G = 10.7 μm in order to demonstrate reproducibility. Figure S7 shows further load-displacement curves for different pore sizes and different punch sizes. For a target displacement of 1200 nm, the increase in load after the first failure is due to the increase in contact area related to the conical shape of the indent, and the arrest displacement after the burst is nominally the size of the template sphere. Inspection of the residual contact impressions reveals a sufficiently plan-parallel contact between the indenter and sample surface. Even in the case of an indentation to approximately 1 μm using the largest punch diameter of D_G = 54.5 μm, a uniform contact perimeter results, as shown in Fig. 5a. While the microcompression tests led to catastrophic failure of the IO structure, examination of the indented area shows that the surface of the IO structure remains intact while a random distribution of pores are filled with debris resultant from fracture from below.

Fig. 6b shows two typical load-displacement curves associated with flat punch indentation into the 34 nm titania coated IO structure with pore size of D_μ = 756 nm for two different punch diameters of D_G = 5.5 μm and D_G = 10.7 μm. It is observed that the loading stiffness is higher for larger flat punch diameter, as expected, both curves show 2 displacement bursts of similar size. This is consistent with the pore size (in both cases D_μ = 756 nm) controlling the bursts. Another important observation it that while the uncoated samples display a circular residual contact perimeter, the titania coated samples show a contact perimeter that seems to follow the crystallographic directions <011> of the (111) plane (compare Figs. 5d and 6b).

As mentioned in the experimental section, the typical analysis of flat punch indentation data follows the Sneddon approach. While the mean pressure assessed from load-displacement data is simply the ratio of the load to contact area – a value which comes from the geometry of the indenter and depth of indentation, the assessment of the elastic modulus using the Sneddon solution relies on the assumption of contacting a homogeneous half-space. In the case of flat punch indentation into the IO structures, the high stiffness of the underlying substrate will lead to a significantly overestimation of the modulus of the IO coating itself. However, if the load-bearing capacity is limited to the contact regime and the coating thickness, we can treat the load displacement data similarly to uniaxial compression data. That is to say, the modulus is computed as $E_{CSM} = S_{CSM}\,(H/A)$, where H is the thickness of the coating and A is the area of the circular flat punch. The computed stress versus displacement curves and elastic modulus versus strain curves are shown in Figure S4 and S6. The results from all flat punch indentation tests are given in Table 2.

4. Discussion

4.1. Effect of loading mode: compression versus flat punch indentation

Since the advent of hardness testing, efforts have been made to find equivalencies between results from indentation and uniaxial loading modes. In typical sharp tip indentation experiments of fully dense

Table 1
Summary of compression experiments, including standard deviations of computed values.

D_μ nm	Area μm^2	D_G μm	D_G/D_μ	Number of measurements	Strength MPa	$E_{loading,\ max}$ GPa	E_{CSM} GPa
756	5.7 ± 0.4	2.7 ± 0.1	3.6 ± 0.1	3	98.5 ± 11.3	5.3 ± 0.7	6.8 ± 0.9
	25.6 ± 3.5	5.7 ± 0.4	7.5 ± 0.5	3	53.4 ± 7.8	2.5 ± 0.1	2.7 ± 0.2
	107.0 ± 25.2	11.6 ± 1.4	15.4 ± 1.8	3	41.3 ± 2.3	1.7 ± 0.1	1.4 ± 0.2
	251.5 ± 60.5	17.8 ± 2.2	23.6 ± 3.0	3	45.7 ± 6.2	0.9 ± 0.1	1.5 ± 0.1
756 (coated with 34 nm TiO_2)	4.1 ± 0.4	2.3 ± 0.1	3.0 ± 0.1	3	512.5 ± 28.7	14.0 ± 0.9	15.1 ± 0.3
	21.6 ± 1.7	5.2 ± 0.2	6.9 ± 0.3	3	363.0 ± 47.4	7.7 ± 1.0	8.9 ± 0.7
	76.8 ± 8.8	9.9 ± 0.6	13.1 ± 0.7	5	410.0 ± 31.4	8.3 ± 0.7	7.9 ± 0.6
	328.3 ± 7.0	20.4 ± 0.2	27.0 ± 0.3	2	384.0 ± 5.2	4.7 ± 0.1	5.9 ± 0.1

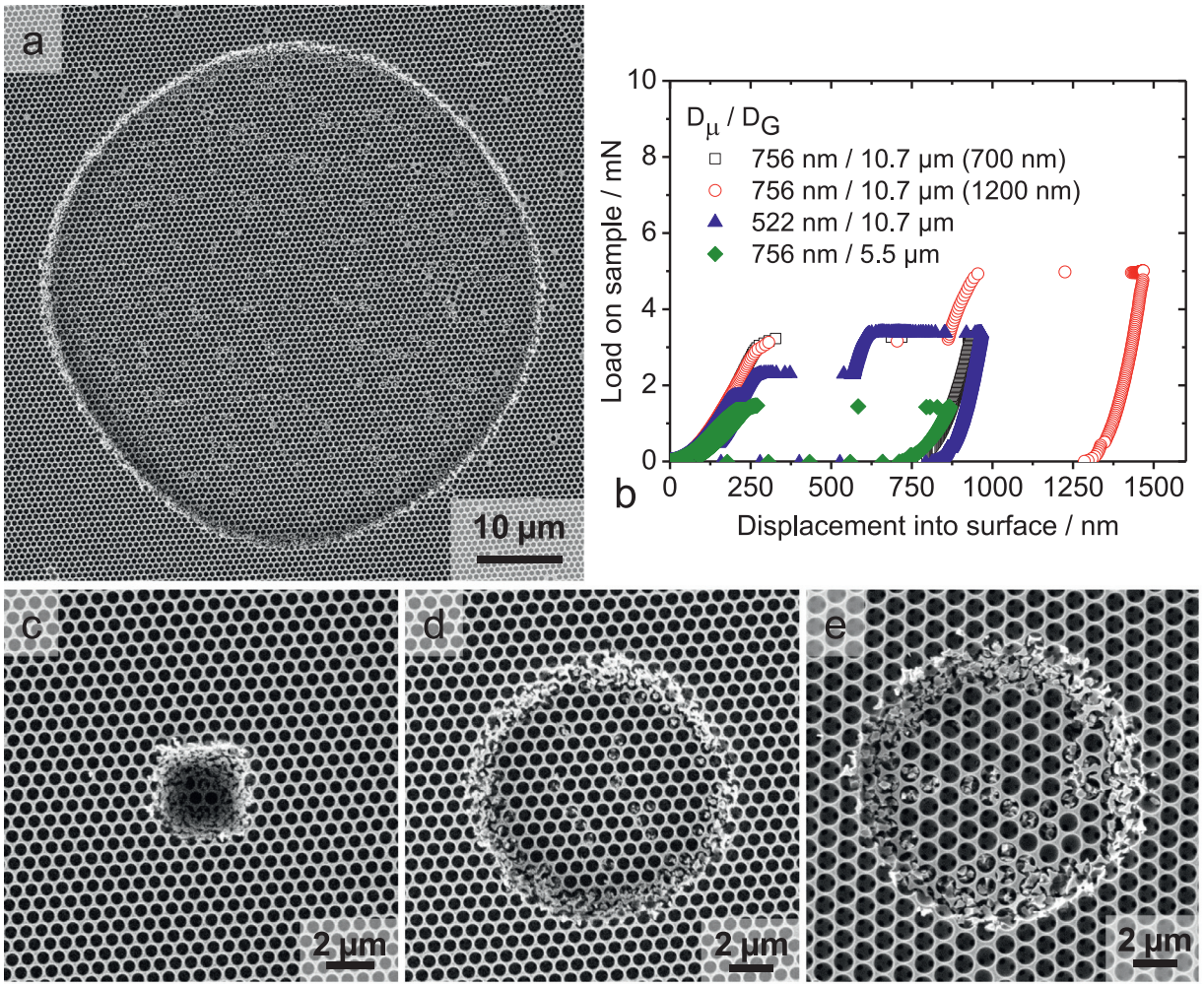

Fig. 5. Results from flat punch indentation of uncoated IO: a) SEM image of residual indent with D_G = 54.5 μm on the surface of the uncoated silica IO sample fabricated with template spheres of D_μ = 756 nm show a uniform depth at the contact perimeter demonstrating good loading alignment. b) Typical load versus displacement curves on uncoated silica IO for D_G = 10.7 μm and D_μ = 756 nm, D_G = 10.7 μm and D_μ = 522 nm, and D_G = 5.5 μm and D_μ = 756 nm. Two different prescribed maximum depths were chosen for D_G = 10.7 μm with D_μ = 756 nm to show reproducibility and the step-like response is due to the consecutive failure of pore layers. c-e) Flat punch indents on the surface of the uncoated silica IO fabricated with template spheres of c) D_μ = 756 nm and D_G = 2.5 μm and d) D_μ = 756 nm and D_G = 10.7 μm and e) D_μ = 1030 nm and D_G = 10.7 μm.

materials, the uniaxial yield strength has been shown to scale as approximately 1/3 of the hardness [18,19]. In the case of elastic modulus measurements, the challenges associated with the accurate assessment of the evolving contact area with indentation displacement have been largely overcome using a variety of techniques. However, the use of these approaches still rely on a reasonable assumption of contacting a homogeneous half-space. The need for characterizing the mechanical properties of thin films, where an equivalent uniaxial constitutive law is often the goal, have driven a lot of the developments of nanoindentation techniques and analyses, where such a homogeneous half-space

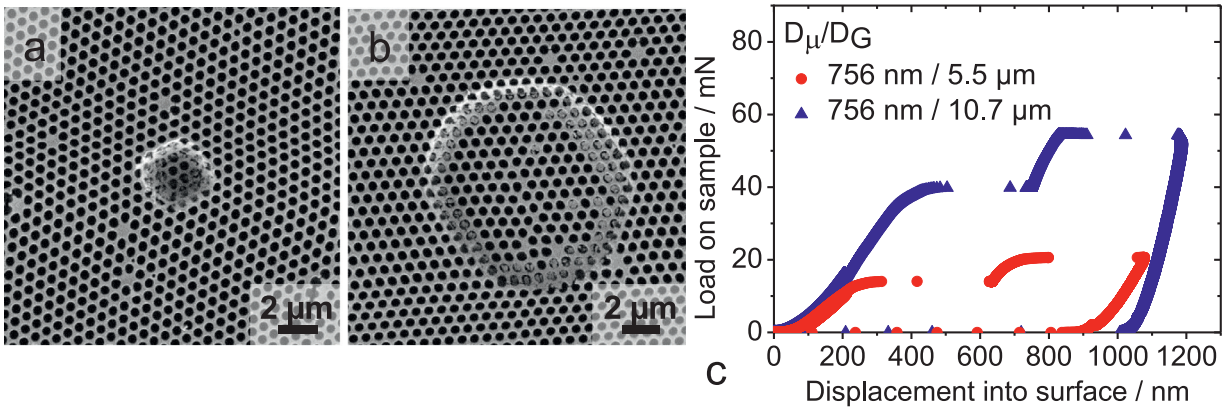

Fig. 6. Results from flat punch indentation of coated IO: SEM image after flat punch indentation on silica IO fabricated with template spheres of D_μ = 756 nm and coated with 34 nm of amorphous titania with a) D_G = 2.5 μm and b) D_G = 10.7 μm. c) Typical load versus displacement curves for varying D_G with D_μ = 756 nm. The displacement bursts correspond to the failure of individual layers, leading to the step-like response.

Table 2
Summary of flat punch indentation experiments, including standard deviations of computed values.

D_μ nm	Area μm^2	D_G μm	D_G/D_μ	Number of measurements	Strength MPa	$E_{uniaxial}$ GPa
198	4.7	2.5	12.4	9	43.7 ± 5.6	1.9 ± 0.2
	23.5	5.5	27.6	9	38.2 ± 6.9	1.9 ± 0.4
522	4.7	2.5	4.7	9	58.0 ± 14.5	3.7 ± 0.4
	23.5	5.5	10.5	9	53.4 ± 8.4	2.7 ± 0.2
	90.7	10.7	20.6	9	25.3 ± 4.6	1.5 ± 0.2
	2330	54.5	37.0	9	29.0 ± 1.3	2.0 ± 0.1
756	4.7	2.5	3.2	9	86.8 ± 10.9	3.5 ± 0.3
	23.5	5.5	7.2	7	59.6 ± 6.3	2.5 ± 0.2
	90.7	10.7	14.2	9	39.2 ± 4.7	1.5 ± 0.2
	179	15.1	20.0	6	39.0 ± 1.0	1.6 ± 0.1
	294	19.4	25.6	9	40.0 ± 4.1	1.4 ± 0.2
	2330	54.5	72.0	9	38.3 ± 5.1	1.4 ± 0.1
1030	23.5	5.5	5.3	9	75.9 ± 6.8	2.4 ± 0.4
	90.7	10.7	10.4	9	54.4 ± 3.9	1.5 ± 0.1
	294	19.4	18.8	9	39.8 ± 1.4	1.3 ± 0.1
	2330	54.5	52.9	9	43.4 ± 2.4	1.2 ± 0.0
756 (coated with 34 nm TiO_2)	4.7	2.5	3.2	6	772 ± 118	21.5 ± 2.0
	23.5	5.5	7.2	9	568 ± 32	12.6 ± 0.5
	90.7	10.7	14.2	8	410 ± 32	8.0 ± 0.1
	179	15.1	20.0	6	473 ± 38	8.1 ± 0.2
	294	19.4	25.6	6	525 ± 13	7.7 ± 0.3
	2330	54.5	72.0	8	612 ± 18	4.1 ± 0.1

assumption no longer holds. The additional complexity of assessing the constitutive mechanical response of highly porous coatings on substrates is less advanced. But interestingly, the porosity may allow a great simplification of the analysis using flat punch indentation testing. If the load sharing capacity of a porous material is limited by the lack of constraint due to the pores, the loading tends toward uniaxial stress state, and thus the mean pressure can be taken as the strength [20] and the strain is simply the displacement over the coating thickness. By applying this approach to the data, the results from the compression and indentation tests are found to be nearly the same, by comparison of Tables 1 and 2.

The main difference in the behaviour between compression and indentation is found in the catastrophic nature of failure in the case of compression, while an arrest displacement of is found for indentation. The step-like bursts observed in the flat punch indentation data reflect the increase in contact area associated with a flat-ended conical indenter, which helps to mitigate failure of the entire coating which occurs during microcompression. The size of the bursts reflect how far a failure event can propagate, which is observed to correspond to the pore size. This is shown in Fig. 5, where the burst size is significantly smaller for the smaller pore size of 522 nm in comparison to the 756 nm pore size results, while the burst size is approximately the same for the 756 nm pore size results where the flat punch diameter varies by approximately a factor of 2.

While the SEM images of the surface of the indents show no fracture or crack propagation outside the punch area, it is of interest to understand the deformation characteristics below the contact. To this end, FIB milling was used to investigate a cross section through an indent associated with 15.1 μm diameter flat punch (D_G) indent in an uncoated silica IO to a prescribed maximum depth of 1200 nm depth. Inspection with SEM (Fig. 7) revealed fracture at the edge of contact into the IO at an angle of 60°, likely due to the conical indenter geometry. No sign of crack propagation or fracture outside the indent area is found. Horizontal cracks through the structure are readily observed below the surface, in-plane cracking is also found, perhaps resulting from crack deflection from below.

4.2. Size effects: influence of pore size (D_μ) and deformation size (D_G)

Size effects in mechanical behaviour have been well known for decades, or longer. It is well established that microstructural length-scales influence the strength of the material, and that the relative density of porous solids impacts the elastic modulus. Less established is how the distribution of microstructural length-scales interplay with sample size on mechanical response. In the present study, both microstructural length-scale and sample size are varied, through the use of different pore (i.e., template sphere) sizes and pillar or flat punch diameters, respectively.

The explicit influence of pore size on the strength can be assessed from the results of the flat punch indentations into uncoated silica IOs fabricated with template spheres of D_μ = 198, 522, 756 and 1030 nm diameter, and two different flat punch diameters of D_G = 5.5 μm and 10.7 μm, as shown in Fig. 8a. It should be noted that compression tests were only carried out on the 756 nm template structures, and therefore only indentation data are presented here. Interestingly, the plot shows an apparent effect of pore size; the strength increases with increasing D_μ. This is opposite of the usual microstructural size effects in strength observed for single crystalline metals which show very strong size effects, i.e. smaller is stronger. Inspection of Fig. 8a, however, also shows a dependence on the flat punch size, D_G; the data shifts to higher strengths for increasing punch diameter. In order to better consider the explicit effect of flat punch diameter, Fig. 8b shows the strength as a function of D_G for two different pore sizes, D_μ = 522 and 756. Here, no clear trend is observed in D_G, but a clear increase in strength is found for an increase in pore size D_μ.

In order to consider the coupled influence of pore size, D_μ, and deformation size, D_G, the ratio D_G/D_μ is used as a characteristic parameter. Fig. 9 shows an overview of all results from compression and indentation experiments on the uncoated structures as a function of D_G/D_μ. The strength as a function of D_G/D_μ for different pore sizes is shown in 9a. The dimensionless parameter D_G/D_μ importantly shows that it is the relative values of the geometric and microstructural length-scales that govern the strength and not the pore size itself; all data from varying pore sizes collapse on the same curve. For all tested pore sizes, a threshold of nominally 40 MPa at $D_G/D_\mu \sim 13$ was found. For $D_G/D_\mu > 13$, the strength stays constant at about 40 MPa for both indentation and compression experiments. Conversely, for $D_G/D_\mu < 13$, the strength increases with decreasing D_G/D_μ, with a more pronounced increase for micropillar experiments (up to 130 MPa) and less pronounced increase for indentation (up to 90 MPa). As was found for the strength, the modulus shows a plateau at around $D_G/D_\mu \sim 13$ for all tested pore sizes, with a value around 1.5 GPa (Fig. 9b), and an even greater increase with for $D_G/D_\mu < 13$

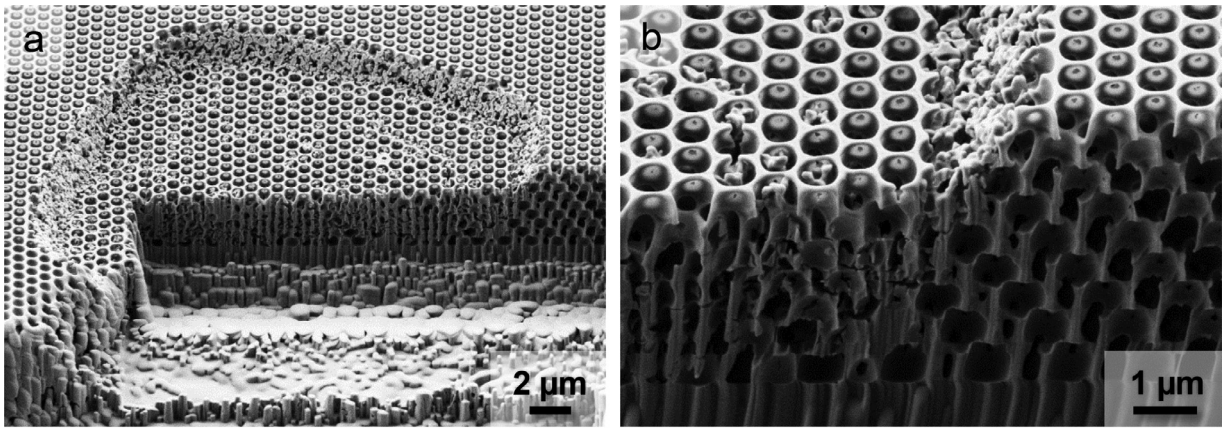

Fig. 7. Fracture below the contact in uncoated silica IO: SEM images of a FIB cross section of an indent made with a flat punch diameter of D_G = 15.1 μm on an uncoated silica IO. a) Overview and b) close up on the edge of the indent shows fracture constrained to within the contact zone; the region outside the indent area remains fully intact.

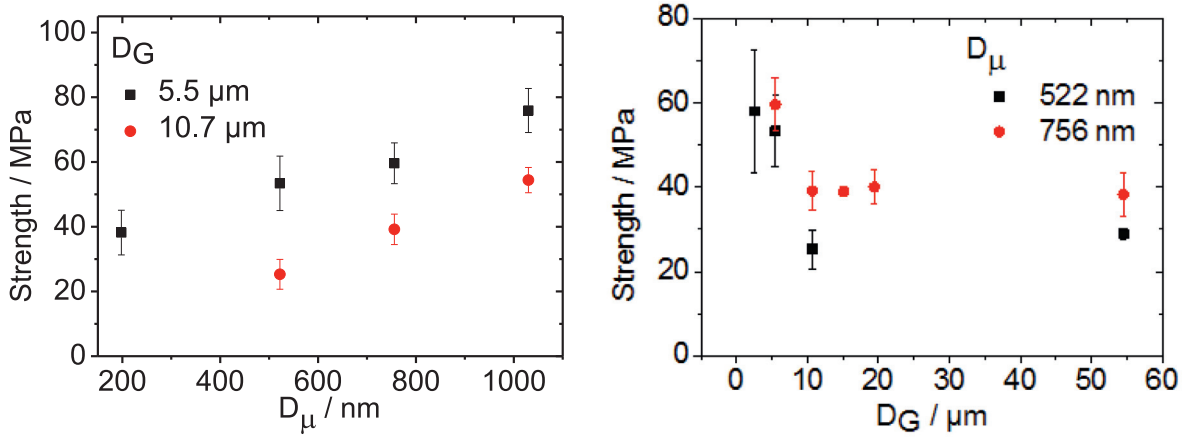

Fig. 8. Size dependencies on strength: (a) Strength vs. D_μ from flat punch indentation data for two different flat punch diameters, D_G = 5.5 μm (black squares) and 10.7 μm (red circles). (b) Strength vs. D_G from flat punch indentation data for two different pore sizes, D_μ = 522 nm (black squares) and 756 nm (red circles). (For interpretation of the references to colour in this figure legend, the reader is referred to the web version of this article.)

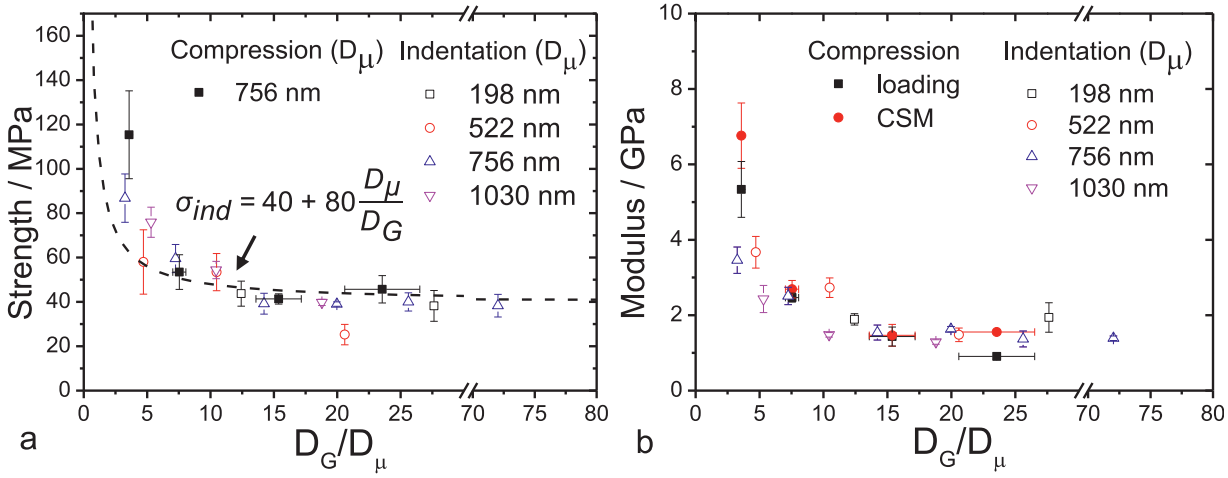

Fig. 9. Comparison between compression and indentation with varying D_G/D_μ. (a) Strength and (b) elastic modulus for uncoated silica IO showing the dependence on the normalized length-scale, D_G/D_μ , and the equivalence of indentation and compression loading. The dashed line represents the model fit of Eq. (4) to the data for the strength of the uncoated IO. The overlap in response indicates a lack in any dependency on the pore size.

relative to the strength response. The basis for these size dependencies can be explained in terms of the porosity and boundary conditions involved, as will now be discussed in greater detail.

For $D_G/D_\mu < 13$, micropillars suffer from redeposition of material during the pillar preparation via FIB milling; milled material infiltrates the pores at the surface leading to a stiffening and strengthening of the smallest pillars, i.e. small D_G. But as the pore size, D_μ is reduced, the ability for material to redeposit into the pore becomes more difficult. Thus it is the ratio of D_G/D_μ that governs the size effect, rather than either absolute length-scale. For $D_G/D_\mu > 13$, all micropillars tend to keep the same strength because the influence of redeposition from milling becomes negligible relative to the sample size. This effect becomes less pronounced with increasing D_G because the perimeter scales linearly and the area squared with the diameter, while the effect decreases with decreasing D_μ since material infiltration becomes more difficult with smaller pore size.

Previous experimental and simulation studies on stochastic metallic foams with millimetre size cells [20,21] and on comparable honeycomb cells have also shown an effect of the specimen size, L, relative to the cell size, d, in both compression and indentation, where the ratio L/d is equivalent to the ratio D_G/D_μ used here. This type of size effect must be separated from effects giving rise to size-dependent strengthening mechanisms, which govern the exceptional mechanical response often observed in fully dense materials. Indeed, no dislocation processes can be considered in the deformation of the amorphous silica based IO structures here.

In compression, it has already been shown that stochastic metallic foams [20,21] and honeycomb cells [21,22] show an increase in strength and modulus with increasing L/d up to a plateau level matching bulk values. This effect of reduced strength and modulus at low L/d is explained by the decreased constraint of cell walls at free surface, making the surface cells more compliant; and by the increased area fraction of cut cell walls at the boundary, which remains stress-free [20,21]. This trend is contrary to the observations made for the IO pillars; in the case of micropillars of open porous material prepared with FIB milling, redeposition into the outer pore layer can occur, leading to a stiffening of the samples at the smallest micropillar sizes. The amount of redeposition will be low for the smallest pore sizes (small D_μ), and the influence of such redeposition will decrease with increasing pillar sizes (large D_G). However, for large D_G/D_μ the properties stabilize at a plateau level as for stochastic metallic foams, no longer influenced by either redeposition or free surfaces.

In the case of indentation into stochastic metallic foams [20,21] and honeycomb cells [21,22], the strength is shown to increase with decreasing L/d, as was found in the IO coatings. They argue that rather than being associated with an intrinsic size effect in the strength of the material, the increase is due to the constraint of the surrounding material outside of the contact. Following their analytical approach, we consider the effect of material constraint on the strength of the pure silica IO structure. The total load on the indenter at fracture initiation, F_{ind} is taken as the sum of the load required to crush the material, F_{crush} and the load required to tear the cell walls at the perimeter of the indenter, F_{tear}. F_{crush} is equal to the bulk strength of the foam, σ_{bulk}, times the cross sectional contact area, $A = (\pi {D_G}^2)/4$ and F_{tear} is equal to the shear strength of the foam, τ_{bulk}, times the product of the contact perimeter, πD_G, and the depth over which shearing occurs, kD_μ, where k gives the number of cells over which shearing occurs at the edge of the indenter:

$$F_{ind} = F_{crush} + F_{tear} = \frac{\sigma_{bulk}\left(\pi {D_G}^2\right)}{4} + \tau_{bulk}\pi D_G H_{shear}, \tag{2}$$

which can be rewritten in terms of the indentation stress, i.e., the mean pressure of contact:

$$\sigma_{ind} = \sigma_{bulk} + 4k\tau_{bulk}\frac{D_\mu}{D_G}. \tag{3}$$

Inspection of 9a shows that all data converge to a plateau stress of around 40 MPa, which is taken as the value of σ_{bulk} for the uncoated silica IO. Applying the Tresca criterion, τ_{bulk} can be approximated as $\sigma_{bulk}/2$ = 20 MPa. Inspection of the load-displacement curves shown in Fig. 5b reveals a displacement burst of approximately one structural length, D_μ, at the point of fracture. It follows that the parameter k can be taken as 1. Inserting these values for τ_{bulk}, σ_{bulk} and k, into Eq. (3) gives:

$$\sigma_{ind} = 40\,\text{MPa} + 80\,\text{MPa}(D_\mu/D_G), \tag{4}$$

which is plotted against the data in 9a, and shown to describe the data quite well.

4.3. Effect of amorphous titania film

A clear influence of the 34 nm titania film on the mechanical behavior of the IO structures is demonstrated in comparing the results for the microcompression of coated and uncoated samples (Table 1) and for indentation into the coated and uncoated samples (Table 2). In order to make a more systematic comparison of the coated and uncoated samples, inclusive of the influence of loading

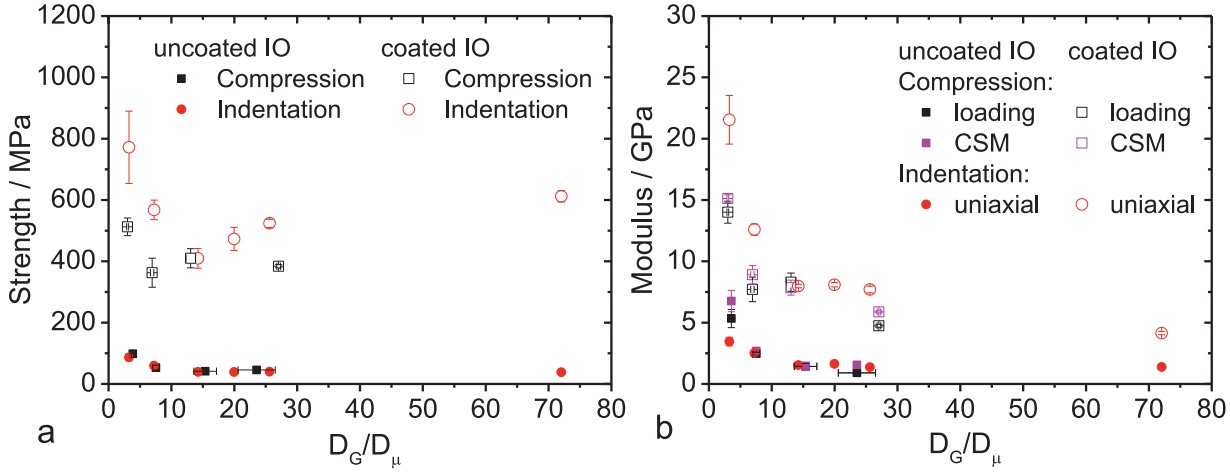

Fig. 10. Influence of titania film on the mechanical response of silica IOs: a) Strength and b) modulus assessed by flat punch indentation (circular symbols) and microcompression (square symbols) of uncoated silica IO (filled symbols) and 34 nm titania coated silica IO (open symbols) as a function of D_G/D_μ. for a fixed pore size of D_μ = 756 nm and varying D_G.

state and size dependencies, Fig. 10 presents the data for the strength and modulus as a function of the characteristic size parameter, D_G/D_μ for the 34 nm amorphous titania coated IO along with the results for the uncoated sample (as presented in Fig. 9). Only data for a pore size of 756 nm (D_μ) is included. Here we differentiate between the results from microcompression and indentation.

Both uncoated and coated IO structures show a decrease in modulus with increasing D_G/D_μ for values up to D_G/D_μ ~ 13, beyond a plateau is reached. This holds for both compression and indentation results, despite the differences in boundary conditions for each loading mode, namely the free surfaces in the case of the pillars, and material constraint at the contact perimeter in the case of indentation. The 34 nm titania film is shown to lead to a 5-fold increase in the elastic modulus, increasing from ~1.5 GPa for the uncoated IO, up to ~8 GPa for the coated IO.

Comparison of the strengths is less straightforward. In the case of the titania coated IOs for $D_G/D_\mu < 13$, the strength increases strongly with decreasing D_G/D_μ, as in the case of the uncoated IO. However, the effect is stronger for the indentation than for compression. This can be understood in terms of the effect of material redeposition during the FIB milling process. Redeposition is more pronounced in the uncoated IO, where the porosity is higher and the holes connecting the pores are larger, allowing more infiltration. The connecting holes in the titania coated IO are so small that redeposition of material is minimized and only influences really small pillars (D_G/D_μ ~ 3). In the case of titania coated IOs at $D_G/D_\mu > 13$, the strength displays a plateau at about 400 MPa for the micropillar compression tests whereas the indentation results show a continued increase in strength. This can be understood in terms of the influence of the load sharing capacity of the IO samples. The addition of a 34 nm titania increases the total solid volume fraction; the sample is denser than the uncoated IO. This would lead to a less appropriate equivalence between the mean pressure (or equivalent hardness) for indentation loading, and that of uniaxial deformation. As mentioned in Section 4.1, the uniaxial yield strength has been shown to scale as approximately 1/3 of the hardness for fully dense materials. An increase in porosity reduces the extent of triaxiality and load sharing capacity, leading to a more uniaxial loading state. Inversely, by increasing the density in the case of the coated IO, we start to deviate from the uniaxial condition for the flat punch indentation, consistent with the deviation of values of strength evaluated for the indentation and compression experiments observed in Fig. 10a.

In order to appropriately compare the strengths for the coated and uncoated sample, we therefore use the plateau value found for the compression experiments. It is found that the 34 nm titania film increased the strength of pure silica IOs from ~40 MPa up to ~400 MPa – a 10-fold increase! When considering the density of the inverse opals (uncoated IO: 330 kg m^{-3} and coated IO: 890 kg m^{-3}) [15], both modulus and strength values are extremely high; these values importantly populate unexplored areas of the design charts.

Beyond the strength and modulus, the titania film also affects the failure behaviour of the IO structures. Compression of the coated IO structures leads to high fracture strengths along with a tougher fracture response; while the uncoated silica IO showed a sort of shattering of the structure, the top of the titania coated IOs remain intact after failure, as shown in Fig. 4d. While the uncoated IO samples fail at displacements smaller than the pore size, the displacement at fracture of the coated IO samples surpasses that of the pore size. This can be observed in comparing Figs. 3 and 4.

In the case of flat punch indentation of coated samples with high ratio of D_G/D_μ (i.e. 25.6 and 72.0), the displacement depths at fracture surpass the size of one layer of pores. In this case, crack propagation or partial fracture of layers occurs prior to a subsequent catastrophic event.

5. Conclusions

The strength and modulus of mechanical metamaterials based on inverse opal coatings were investigated by microcompression and flat punch indentation techniques. A dimensionless parameter, D_G/D_μ, involving geometrical (D_G) and microstructural (D_μ) sizes was established to enable comparison between different testing methods and to consider length-scale effects in mechanical behavior. The agreement between compression and indentation was validated within certain limits of D_G/D_μ, This importantly demonstrates the utility of flat punch indentation testing for quantifying the mechanical behaviour of IO coatings in preference to microcompression; due to the highly porous structure, a sufficiently uniaxial stress state results during flat punch indentation. Compared to microcompression, indentation improves the robustness and statistical relevance of measured properties as it eliminates the effects of pillar preparation artefacts, and decreases testing time; due to material redeposition during FIB milling, microcompression results show an apparent stiffening at small values of D_G/D_μ

A threshold in the parameter D_G/D_μ was found for both indentation and compression. For $D_G/D_\mu < 13$, indentation experiments show an increase in properties due to edge effects at the contact perimeter, while compression tests show the same trend at the same threshold due to redeposition during FIB milling of pillars from porous material. This is opposite to the trend of a decrease in properties at small D_G/D_μ found from compression studies of stochastic metallic foams with millimetre size cells. Yet indentation studies of such stochastic foams show similar trends to those found here for IO structures. The increase in strength and modulus found is well described by the model developed for the foam materials. This allows the influence of geometric constraints to be accounted for, circumventing an erroneous interpretation of intrinsic size effects in the material of interest.

Both indentation and compression tests revealed a lack of dependence on pore size for either strength or elastic modulus. This points to the ability to tailor the photonic properties for a given application without influencing the mechanical response. However, the application of a 34 nm amorphous titania film, as indicated by a characteristic shift in the specular reflection, led to a 10-fold increase in strength and 5-fold increase in elastic modulus of the silica IO structures, while the density is increased by factor of less than 3. This opens the possibility to explore the influence of varying film materials and thicknesses on the mechanical and photonic response of IO structures.

Declaration of Competing Interest

The authors declare that they have no known competing financial interests or personal relationships that could have appeared to influence the work reported in this paper.

Acknowledgements

Funded by the Deutsche Forschungsgemeinschaft (DFG, German Research Foundation) – Projektnummer 192346071 – SFB 986. We thank Dr. Robert Zierold and Martin Waleczek for the ALD films and the thickness measurements of the ALD films and Dr. Alexander Yu. Petrov, Dr. Pavel N. Dyachenko and Prof. Manfred Eich for the optical characterization.

Supplementary materials

Supplementary material associated with this article can be found in the online version at doi:10.1016/j.actamat.2020.04.025.

References

[1] L.R. Meza, A.J. Zelhofer, N. Clarke, A.J. Mateos, D.M. Kochmann, J.R. Greer, Resilient 3D hierarchical architected metamaterials, Proc. Natl. Acad. Sci. USA 112 (2015) 11502–11507 https://doi.org/, doi: 10.1073/pnas.1509120112.

[2] D. Jang, L.R. Meza, F. Greer, J.R. Greer, Fabrication and deformation of three-dimensional hollow ceramic nanostructures, Nat. Mater. 12 (2013) 893 https://doi.org/, doi: 10.1038/nmat3738.

[3] J. Bauer, S. Hengsbach, I. Tesari, R. Schwaiger, O. Kraft, High-strength cellular ceramic composites with 3D microarchitecture, Proc. Natl. Acad. Sci. USA 111 (2014) 2453–2458 https://doi.org/, doi: 10.1073/pnas.1315147111.

[4] J. Bauer, A. Schroer, R. Schwaiger, I. Tesari, C. Lange, L. Valdevit, O. Kraft, Push-to-pull tensile testing of ultra-strong nanoscale ceramic-polymer composites made by additive manufacturing, Extreme Mech. Lett. 3 (2015) 105–112 https://doi.org/, doi: 10.1016/j.eml.2015.03.006.

[5] J. Bauer, A. Schroer, R. Schwaiger, O. Kraft, Approaching theoretical strength in glassy carbon nanolattices, Nat. Mater. 15 (2016) 438 https://doi.org/, doi: 10.1038/nmat4561.

[6] L.R. Meza, S. Das, J.R. Greer, Strong, lightweight, and recoverable three-dimensional ceramic nanolattices, Science 345 (2014) 1322–1326 https://doi.org/, doi: 10.1126/science.1255908.

[7] J.J. do Rosário, E.T. Lilleodden, M. Waleczek, R. Kubrin, A.Y. Petrov, P.N. Dyachenko, J.E.C. Sabisch, K. Nielsch, N. Huber, M. Eich, G.A. Schneider, Self-assembled ultra high strength, ultra stiff mechanical metamaterials based on inverse opals, Adv. Eng. Mater 17 (2015) 1420–1424 https://doi.org/, doi: 10.1002/adem.201500118.

[8] J.-.H. Lee, L. Wang, M.C. Boyce, E.L. Thomas, Periodic bicontinuous composites for high specific energy absorption, Nano Lett. 12 (2012) 4392–4396 https://doi.org/, doi: 10.1021/nl302234f.

[9] J. Rys, L. Valdevit, T.A. Schaedler, A.J. Jacobsen, W.B. Carter, J.R. Greer, Fabrication and deformation of metallic glass micro-lattices, Adv. Eng. Mater. 16 (2014) 889–896 https://doi.org/, doi: 10.1002/adem.201300454.

[10] X. Zheng, H. Lee, T.H. Weisgraber, M. Shusteff, J. DeOtte, E.B. Duoss, J.D. Kuntz, M.M. Biener, Q. Ge, J.A. Jackson, S.O. Kucheyev, N.X. Fang, C.M. Spadaccini, Ultralight, ultrastiff mechanical metamaterials, Science 344 (2014) 1373–1377 https://doi.org/, doi: 10.1126/science.1252291.

[11] X. Wendy Gu, J.R. Greer, Ultra-strong architected Cu meso-lattices, Extreme Mech. Lett. 2 (2015) 7–14 https://doi.org/, doi: 10.1016/j.eml.2015.01.006.

[12] L.C. Montemayor, J.R. Greer, Mechanical response of hollow metallic nanolattices: combining structural and material size effects, J. Appl. Mech. 82 (2015) 71012 https://doi.org/, doi: 10.1115/1.4030361.

[13] V.S. Deshpande, M.F. Ashby, N.A. Fleck, Foam topology: bending versus stretching dominated architectures, Acta Mater. 49 (2001) 1035–1040 https://doi.org/, doi: 10.1016/S1359-6454(00)00379-7.

[14] V.S. Deshpande, N.A. Fleck, M.F. Ashby, Effective properties of the octet-truss lattice material, J. Mech. Phys. Solids 49 (2001) 1747–1769 https://doi.org/, doi: 10.1016/S0022-5096(01)00010-2.

[15] J.B. Berger, H.N.G. Wadley, R.M. McMeeking, Mechanical metamaterials at the theoretical limit of isotropic elastic stiffness, Nature 543 (2017) 533–537 https://doi.org/, doi: 10.1038/nature21075.

[16] B. Hatton, L. Mishchenko, S. Davis, K.H. Sandhage, J. Aizenberg, Assembly of large-area, highly ordered, crack-free inverse opal films, Proc. Natl. Acad. Sci. USA 107 (2010) 10354–10359 https://doi.org/, doi: 10.1073/pnas.1000954107.

[17] G. Shang, K.P. Furlan, R. Zierold, R.H. Blick, R. Janßen, A. Petrov, M. Eich, Transparency induced in opals via nanometer thick conformal coating, Sci. Rep. 9 (2019) 11379 https://doi.org/, doi: 10.1038/s41598-019-47963-2.

[18] D. Tabor, The Hardness of Metals, Clarendon Press, Oxford, UK, 1951.

[19] K.L. Johnson, Contact Mechanics, Cambridge University Press, Cambridge, 1985.

[20] E.W. Andrews, G. Gioux, P. Onck, L.J. Gibson, Size effects in ductile cellular solids. Part II: experimental results, Int. J. Mech. Sci. 43 (2001) 701–713 https://doi.org/, doi: 10.1016/S0020-7403(00)00043-6.

[21] P.R. Onck, Scale effects in cellular metals, MRS Bull. 28 (2003) 279–283.

[22] P.R. Onck, E.W. Andrews, L.J. Gibson, Size effects in ductile cellular solids. Part I: modeling, Int. J. Mech. Sci. 43 (2001) 681–699 https://doi.org/, doi: 10.1016/S0020-7403(00)00042-4.